

Article

Topology Optimization with Matlab: Geometrically Non-Linear Optimum Solid Structures at Random Force Strengths

Marek Werner ^{*}, Sören Bieler and Kerstin Weinberg

Chair of Solid Mechanics, University of Siegen, Paul-Bonatz-Str. 9-11, 57076 Siegen, Germany

* Correspondence: marek.werner@uni-siegen.de; Tel.: +49-271-740-4644

Abstract: This paper aims to investigate multiple large-strain topology-optimized structures, by interpreting their overlay as a probability density function. Such a strategy is suited to finding an optimum design of silicon electrodes subject to a random contact. Using this method, and prescribing a zero net-force constraint on the global system, the optimum structure is identified with a Schwarz P minimum-surface structure. Then, the optimum structure is subject to chemo-mechanically coupled cycling, in terms of an irreversible thermodynamic process, which shows the interplay between the mechanical and chemical fields. The Matlab-based optimization code is attached.

Keywords: topology optimization; Schwarz P surface; geometric non-linearity; finite strain

1. Introduction

More than 60 years ago, Lucien Schmit [1] studied how to combine optimization techniques with the finite element method (FEM), and later, Bense and Kikuchi reported their seminal paper [2]. Since then, topology optimization techniques have been typically used in lightweight design [3–7], where only a percentage of a given volume is occupied by material, while meeting similar overall system stiffness requirements as the entire body. Technological advances in additive manufacturing in particular, make it possible to create structures that exceed conventional design [8]. However, optimum designs result predominantly from prescribed static boundary condition problems [9,10], even if the superordinate system is based on dynamic motion, e.g., a bicycle chain [11]. In such a system, a tensile force acts on the individual link of the chain. The optimum shape of a plate shows the positions for the bolted connections, see Figure 1. The resulting structure might be subject to a low volume constraint, so recent optimization algorithms also account for, e.g., buckling [12], fracture [13], or multi-material demands [14]. In addition, the optimum structure might be part of a periodic structure (the chain) [15], and other manufacturing constraints could be implemented by a projection-based approach [16].

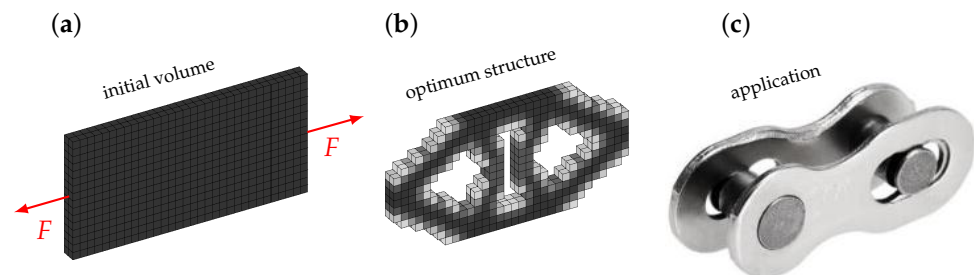


Figure 1. Optimizing a plate subjected to opposite forces at both ends leads to a bicycle chain link. In (a), the initial volume is shown, (b) shows the optimum material distribution, and (c) is the technical application.



Citation: Werner, M.; Bieler, S.; Weinberg, K. Topology Optimization with Matlab: Geometrically Non-Linear Optimum Solid Structures at Random Force Strengths. *Solids* **2023**, *4*, 94–115. <https://doi.org/10.3390/solids4020007>

Academic Editor: Fabrizio Dolcini

Received: 1 March 2023

Revised: 22 March 2023

Accepted: 24 March 2023

Published: 29 March 2023



Copyright: © 2023 by the authors. Licensee MDPI, Basel, Switzerland. This article is an open access article distributed under the terms and conditions of the Creative Commons Attribution (CC BY) license (<https://creativecommons.org/licenses/by/4.0/>).

However, while it is similar, it is also different from the silicon (Si) electrode particles in batteries, which are exposed to large deformations. According to [17], up to now, only a few structural designs, such as porous, core-shell, yolk-shell, and solid nanostructures, have been proposed for silicon anodes, some of them inspired by nature. However, recently, the topology optimization of electrodes has gained more and more attention [18,19]. For the anode design and the improvement of its electrochemical performance, it is crucial to identify the repeated volume expansions (up to about 300% [20]) and contractions during lithiation and de-lithiation, as the key failure mechanism of Si. Particle swelling leads to structural pulverization, electrical disconnection between the active materials and the current collector, continuous exfoliation, and consumption of the active Si and electrolyte of active Si particles [17,21,22]. All these failures can be assigned to the topology of the anode: (i) the increased consumption of the electrolyte (side reactions) could be related to a high surface area, (ii) a materials-dependent fracture occurrence above a specific particle size, and (iii) electrical conductivity issues due to point-to-point contact. As a result of the swelling, interactions with adjacent particles occur randomly, as shown in Figure 2. Most recently, contact has been added to the optimization, e.g., by [23–26]. Moreover, it was found that the contact stress is in the range of diffusion-induced stress under the free-expansion state [27].

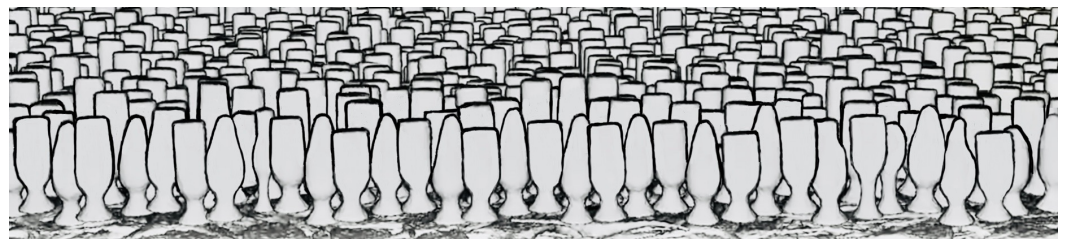


Figure 2. Sketch of silicon particle contact during lithiation. The initially cylindrical rods swell over time to balloon-shaped objects, and might touch each other.

A topology optimization problem is generally solved when finding the optimum material distribution subject to specific demands such as maximum stiffness, maximum conductivity, or others. The common algorithms rely on the finite element method, filtering methods, and the formulation of an optimality criterion [28]. Although numerous techniques exist in the scientific literature, e.g., evolutionary topology optimization (ETO [29]), smooth-edged material distribution for optimizing topology (SEMDOT [30]), floating projection topology optimization (FPTO [31]), etc., there are two popular methods: the Solid Isotropic Material with Penalization (SIMP) method and the Bidirectional Evolutionary Structural Optimization (BESO) method. The SIMP method is the most widely utilized approach, although the BESO method shows a fast convergence rate, with fewer iterations than the SIMP method [32]. In the literature, mainly the optimization problems of a linear-elastic material model are solved [32,33] and some studies address non-linear problems, e.g., [34–36]. Recently, a two-dimensional BESO algorithm for non-linear problems has been reported [32], which claims *one can hardly find convenient and compact published code*.

In this paper, the aim is to elaborate on the BESO approach, in terms of (i) extending the code to 3D, (ii) making it comparable with the Matlab code reported in the SIMP approach [37], (iii) validating the comparability between both approaches for small deformations, (iv) using the BESO approach for random large force interactions as typical in silicon, and (v) defining an optimum structure at large strains by overlapping the single results. Since we are interested in large deformations, we need to recap in Section 2.1, briefly, some continuum mechanics-based essential equations of non-linear elasticity, cf. [38,39]. Then we proceed in Section 2.2 by solving the non-linear equations using FEM. Density-based methods such as BESO and SIMP, and filtering techniques are briefly sketched in Section 2.3. In Section 2.4, we state the optimization problem at large strains. How the resulting structure must be modified to be used in a chemo-mechanically coupled inves-

tigation is sketched in Section 2.5. Finally, we show and discuss the optimum results in Section 3. The 3D non-linear optimization code is provided in Appendix A.

2. Materials and Methods

In the following, we elaborate on the governing equations and the method for solving a non-linear optimization problem. In general, the structure of a software presupposes a certain convention and symbolic expressions, which are declared in the following.

2.1. Continuum Mechanics

Any problem in elasticity is usually based on a strain–displacement relation, a constitutive equation (stress–strain relation), a traction–stress relation, and the formulation of linear and angular balance laws. Since all equations rely on the formulation of the displacement of a material point, we embed it in the environment of continuous media first.

2.1.1. Displacement of Continuous Media

Let \mathbf{X} refer to a point of a continuum in its reference (“material”) configuration $\mathcal{B}_0 \subset \mathbb{R}^3$, and a motion moves the point to its actual (“spatial”) position $\mathbf{x}(\mathbf{X}, t)$ at time t , in the current configuration $\mathcal{B}_t \subset \mathbb{R}^3$. Then, the corresponding displacement vector \mathbf{u} , has the shortest distance between \mathbf{x} and \mathbf{X} , and is defined by their difference as

$$\mathbf{u} = \mathbf{x} - \mathbf{X} \quad \rightarrow \quad \begin{cases} d\mathbf{u} = d\mathbf{x} - d\mathbf{X} & \text{(infinitesimal)} \\ d\mathbf{u} = \mathbf{u}(\mathbf{X} + d\mathbf{X}) - \mathbf{u}(\mathbf{X}) & \text{(finite difference)} \\ \mathbf{u}(\mathbf{X} + d\mathbf{X}) = \mathbf{u}(\mathbf{X}) + (\nabla\mathbf{u})d\mathbf{X} + \dots & \text{(Taylor Series)} \end{cases} \quad (1)$$

From Equation (1), there follows an expression for the differential line element

$$d\mathbf{x} = [\mathbf{1} + \nabla\mathbf{u}] d\mathbf{X} = \mathbf{F} d\mathbf{X} \quad (2)$$

directly, where $\mathbf{1} \in \mathbb{R}^{3 \times 3}$ is the identity matrix and \mathbf{F} the deformation gradient. As usual, variables are denoted with capital letters when referring to the reference configuration. Moreover, the displacement has, in both configurations, the same values but different arguments, $\mathbf{U}(\mathbf{X}, t) = \mathbf{u}(\mathbf{x}, t)$.

2.1.2. Green–Lagrangian Strain Tensor

Both of the differential line elements in Equation (2), $d\mathbf{x}$ and $d\mathbf{X}$, are associated with a differential arc length, and their squares are coordinate-independent quantities. Thus, the difference between the squares of the differential line elements

$$d\mathbf{x} \cdot d\mathbf{x} - d\mathbf{X} \cdot d\mathbf{X} =: d\mathbf{X} \cdot [2\mathbf{E} d\mathbf{X}] \quad (3)$$

is considered as a measure of deformation, and defined as the Green–Lagrangian strain tensor. Together with Equation (2), there follows an expression for the Green–Lagrangian strain tensor

$$\mathbf{E} = \frac{1}{2}[\nabla\mathbf{u} + (\nabla\mathbf{u})^T] + \frac{1}{2}[\nabla\mathbf{u}(\nabla\mathbf{u})^T] = \boldsymbol{\varepsilon} + \boldsymbol{\varepsilon}_N, \quad (4)$$

which is based on the gradient of the displacement. As long as $\|\nabla\mathbf{u}\| \ll 1$ is satisfied, we are in the regime of infinitesimal strain theory, and then the strain tensor composes additively, $\mathbf{E} \approx \boldsymbol{\varepsilon} = \frac{1}{2}(\mathbf{F}^T + \mathbf{F}) - \mathbf{1}$. Otherwise, the strain tensor composes multiplicatively, $\mathbf{E} = \frac{1}{2}(\mathbf{F}^T \mathbf{F} - \mathbf{1})$, and measures how much the right Cauchy–Green tensor $\mathbf{C} = \mathbf{F}^T \mathbf{F}$ differs from $\mathbf{1}$.

2.1.3. Hooke’s Law

In a small strain regime, Hooke’s law for continuous media relates the Cauchy (“true”) stresses $\boldsymbol{\sigma} \in \mathbb{R}^{3 \times 3}$ and the strains $\boldsymbol{\varepsilon} \in \mathbb{R}^{3 \times 3}$ by using a fourth-order elasticity tensor $\mathbf{C} \in \mathbb{R}^{3 \times 3 \times 3 \times 3}$, $\boldsymbol{\sigma} = \mathbf{C}\boldsymbol{\varepsilon}$. Due to the inherent and material symmetries, and the assumption

of isotropic media, the elasticity tensor can be reduced to only two independent Lamé parameters (λ, μ) , and then the Cauchy stresses reads

$$\sigma = 2\mu\varepsilon + \lambda\text{tr}(\varepsilon)\mathbf{1} \quad \text{with} \quad \lambda = \frac{E\nu}{(1+\nu)(1-2\nu)} \quad \text{and} \quad \mu = \frac{E}{2(1+\nu)} \quad (5)$$

Alternatively, the Lamé parameters can be expressed by using the Young’s modulus, E , and Poisson number, ν .

2.1.4. Voigt Notation

Due to the symmetry of the Cauchy stress tensor, $\sigma = \sigma^T$, it can be condensed to an array with six entries. Then, using a superscript V , to indicate Voigt notation, Hooke’s law is rewritten as

$$\sigma = \mathcal{C}\varepsilon \quad \rightarrow \quad \sigma^V = \mathcal{C}^V\varepsilon^V \quad \text{where} \quad \begin{cases} \sigma^V = [\sigma_{11} & \sigma_{22} & \sigma_{33} & \sigma_{23} & \sigma_{13} & \sigma_{12}]^T \\ \varepsilon^V = [\varepsilon_{11} & \varepsilon_{22} & \varepsilon_{33} & 2\varepsilon_{23} & 2\varepsilon_{13} & 2\varepsilon_{12}]^T \end{cases} \quad (6)$$

Alternative arrangements of the off-diagonal stress-tensor entries are possible, e.g., as used by the authors in [37], or given by the Nye notation which is often adapted due to convention in other software coding. However, the elasticity tensor in Voigt notation is dependent on the elasticity constants (E, ν) and partitioned into four 3×3 blocks as

$$\mathcal{C}^V(E, \nu) = \frac{E}{(1+\nu)(1-2\nu)} \begin{bmatrix} A & \mathbf{0} \\ \mathbf{0} & \frac{(1-2\nu)}{2}\mathbf{1} \end{bmatrix} \quad \text{with} \quad A = \begin{bmatrix} 1-\nu & \nu & \nu \\ \nu & 1-\nu & \nu \\ \nu & \nu & 1-\nu \end{bmatrix} \quad (7)$$

where $\mathbf{0} = \mathbf{0}\mathbf{1}$ is a zero matrix.

2.1.5. Cauchy Traction Vector

Now, the stresses (6) are related to infinitesimal acting forces $d\mathbf{f}$ per infinitesimal area of a region da , with outward normal \mathbf{n} to the surface,

$$\sigma\mathbf{n} = \frac{d\mathbf{f}}{da} =: \mathbf{t} \quad (8)$$

both in the spatial configuration, and defined as the Cauchy traction vector \mathbf{t} .

2.1.6. Nanson’s Formula

The force-to-area ratio in Equation (8) refers to quantities in the current configuration. Nanson’s formula links the area in the current configuration da , with its outward normal \mathbf{n} , to the same area in the reference configuration dA , with outward normal \mathbf{N} , by

$$\mathbf{n} da = J\mathbf{F}^{-T}\mathbf{N} dA \quad \text{with} \quad J = \det(\mathbf{F}) = \frac{dv}{dV} \quad (9)$$

The determinant of the deformation gradient J , is the ratio of the volume elements dv and dV , from the actual and reference configurations.

2.1.7. Static Equilibrium

With Equation (9) at hand, the transformations of the area and volume elements from the actual to the reference configuration are given. Let $\partial\mathcal{B}_t$ denote a surface within or on the boundary of \mathcal{B}_t . Then, the total force acting on this surface is given by

$$\mathbf{f} \stackrel{(8)}{=} \int_{\partial\mathcal{B}_t} \mathbf{t} da \stackrel{(8)}{=} \int_{\partial\mathcal{B}_t} \sigma\mathbf{n} da \stackrel{(9)}{=} \int_{\partial\mathcal{B}_0} J\sigma\mathbf{F}^{-T}\mathbf{N} dA \stackrel{(D)}{=} \int_{\mathcal{B}_0} \nabla \cdot \mathbf{P} dV \quad (10)$$

where the Cauchy traction vector (8), the Nanson formula (9), the divergence theorem (D), and the definition for the 1st Piola–Kirchhoff stress tensor

$$\mathbf{P} = J\boldsymbol{\sigma}\mathbf{F}^{-T} \quad (11)$$

have been used. \mathbf{P} relates the forces f , in the spatial configuration, with areas in the material configuration. The forces f , can be assigned with a spatial body force density \mathbf{b} ,

$$\mathbf{f} = \int_{\mathcal{B}_t} \mathbf{b} \, dv = \int_{\mathcal{B}_0} J\mathbf{b} \, dV \quad \text{where} \quad \mathbf{b} = \frac{d\mathbf{f}}{dv} \quad \text{and} \quad \tilde{\mathbf{B}} = J\mathbf{b} \quad (12)$$

With Equations (10)–(12), the static equilibrium equation reads in differential form

$$\nabla \cdot \mathbf{P} - \tilde{\mathbf{B}} = \mathbf{0} \text{ (quasi-static balance of linear momentum)} \quad (13)$$

with boundary conditions

$$\mathbf{P}\mathbf{N} = \bar{\mathbf{T}} \quad \text{on } \partial\mathcal{B}_T \quad \text{(Neumann boundary condition)} \quad (14)$$

$$\mathbf{u} = \bar{\mathbf{u}} \quad \text{on } \partial\mathcal{B}_u \quad \text{(Dirichlet boundary condition)} \quad (15)$$

where $\partial\mathcal{B}_0 = \partial\mathcal{B}_u \cup \partial\mathcal{B}_T$ with $\partial\mathcal{B}_u \cap \partial\mathcal{B}_T = \emptyset$, and the quantities with a bar are prescribed. Moreover, the 2nd Piola–Kirchhoff stress tensor

$$\mathbf{S} = \mathbf{F}^{-1}\mathbf{P} \quad (16)$$

relates forces in the reference configuration to areas in the reference configuration.

2.1.8. Hyperelastic Material Model

For a hyperelastic material, the stress tensor (5) is derived from a strain energy density function Ψ ,

$$\boldsymbol{\sigma} = \frac{\partial\Psi_\varepsilon}{\partial\varepsilon} \quad \text{where} \quad \Psi_\varepsilon = \frac{1}{2}\lambda(\text{tr}(\boldsymbol{\varepsilon}))^2 + \mu \text{tr}(\boldsymbol{\varepsilon}^2) \quad (17)$$

However, it is known that $\boldsymbol{\sigma}$ is variant to pure rotations, while $\boldsymbol{\varepsilon}$ is not. Therefore, it is not suited as a constitutive model for large deformations. In the case of finite deformations, instead of $\boldsymbol{\sigma}$, often the 2nd Piola–Kirchhoff stress tensor \mathbf{S} is used,

$$\mathbf{S} = \frac{\partial\Psi_E}{\partial\mathbf{E}} = 2\frac{\partial\Psi_E}{\partial\mathbf{C}} \quad \text{where} \quad \Psi_E = \frac{1}{2}\lambda(\text{tr}(\mathbf{E}))^2 + \mu \text{tr}(\mathbf{E}^2) = \Psi_\varepsilon + \Psi_\Delta \quad (18)$$

In Equation (18), the most straightforward hyperelastic strain energy density is formulated, i.e., the Saint Venant–Kirchhoff model, which is an extension of Equation (17). This gives $\mathbf{S} = 2\mu\mathbf{E} + \lambda\text{tr}(\mathbf{E})\mathbf{1}$, which is similar to Equation (5). The limitations of the Saint Venant–Kirchhoff material model in large strain regimes are discussed in [40]. Alternatively, many other strain energy density formulations, such as the Ogden model [41,42], neo-Hookean model, Money–Rivlin model, Simo–Pister model [43], etc., could be adapted to match with a specific material behavior of interest.

2.1.9. Non-Linear Hookes Law

In the case of non-linear strain, the 2nd Piola–Kirchhoff stress tensor in Voigt notation

$$\mathbf{S}^V = \mathbf{C}\mathbf{E}^V \quad \rightarrow \quad \boldsymbol{\sigma}^V = \mathbf{C}\boldsymbol{\varepsilon}^V \quad \text{at small strains} \quad (19)$$

has a similar form to Equation (6), and for infinitesimal deformations, the difference between the Cauchy and Piola–Kirchhoff stress tensors is marginal. The strain in Equation (19) has the components

$$E_{ij} = \frac{1}{2}[\partial_i u_j + \partial_j u_i + \partial_i u_1 \partial_j u_1 + \partial_i u_2 \partial_j u_2 + \partial_i u_3 \partial_j u_3] \equiv E_{ji} \quad (20)$$

with indices as they are arranged for $\boldsymbol{\varepsilon}^V$ in Equation (6).

2.2. Finite Element Analysis

Having formulated S in (18), the transformation of S to P in (16), and the equilibrium Equation (13) on the reference domain \mathcal{B}_0 , it is now discretized into n_{el} elements within the finite element analysis. In the following, the weak form of the problem (13) is formulated, ansatz functions are declared, and the Newton–Raphson method is used to solve the non-linear problem.

2.2.1. Weak Form of Problem

As usual, the multiplication of Equation (13) with a smooth test function vector λ , and integration over the domain \mathcal{B}_0 , gives

$$\int_{\mathcal{B}_0} \lambda \cdot \tilde{B} dV \stackrel{(13)}{=} - \int_{\mathcal{B}_0} \lambda \cdot (\nabla \cdot P) dV \stackrel{(PI)}{=} \int_{\mathcal{B}_0} (\nabla \lambda) : P dV \stackrel{(16)}{=} \int_{\mathcal{B}_0} (F^T \nabla \lambda) : S dV \quad (21)$$

where (PI) denotes partial integration, the Frobenius inner product reads $A : B = \text{tr}(A^T B)$, the trace of a product $\text{tr}(A^T B) = \text{tr}(B A^T)$, and the test function vector λ is chosen so that it vanishes at the boundary $\partial \mathcal{B}_u$. The integral expression in Equation (21) is called the weak form of the problem.

2.2.2. Element ID, Connectivity, and Edof

As in the simplest case, the reference geometry is assumed to be a cuboid to solve Equation (21). This reference cuboid is subdivided into (n_1, n_2, n_3) equidistant elements, such that the total number of elements is $n_{el} = n_1 n_2 n_3$. The elements are numbered successively along the X_1 , then the X_2 , and lastly the X_3 direction, see Figure 3a.

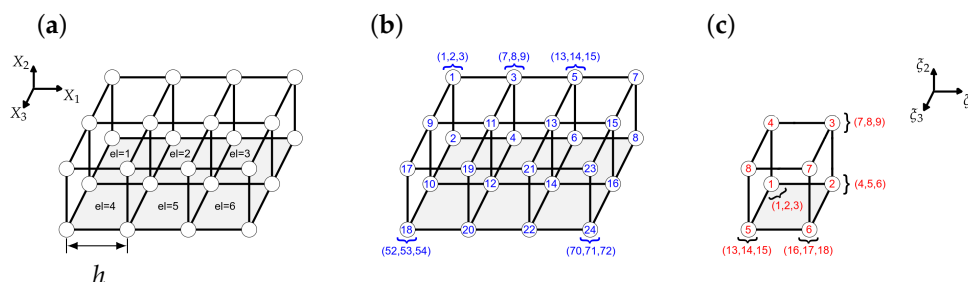


Figure 3. (a) Element ID, (b) global connectivity, and (c) local connectivity.

Each node, which is a corner stone of an element, has three degrees of freedom (dof). Therefore, one element has in total $8 \cdot 3 = 24$ dofs and the total number of dofs is $n_{dof} = 3(n_1 + 1)(n_2 + 1)(n_3 + 1)$. According to [37], the global node identification is ordered column-wise, with the rule: up-to-bottom, left-to-right, and back-to-front, see Figure 3b. The local node identification of the eight nodes within a single element does not necessarily follow the same convention, and is ordered in counter-clockwise direction instead, see Figure 3c. The global connectivity of each single local element, i.e., the mapping of the blue circled numbers to the red circled numbers, is stored for each element (index “el”) within an array

$$\text{edof}_{el} = [\text{node}_{1x} \text{ node}_{1y} \text{ node}_{1z} \text{ node}_{2x} \dots \text{node}_{8z}]^T \in \mathbb{N}^{24} \quad (22)$$

e.g., $\text{edof}_1 = [4, 5, 6, 10, 11, 12, 7, 8, 9, 1, 2, 3, 28, 29, 30, 34, 35, 36, 31, 32, 33, 25, 26, 27]^T$. With this at hand, the nodal values of the local displacement vector

$$\mathbf{u}_{el} = \underline{\mathbf{u}}(\text{edof}_{el}) \in \mathbb{R}^{24} \quad \text{and} \quad \lambda_{el} = \underline{\lambda}(\text{edof}_{el}) \in \mathbb{R}^{24} \quad (23)$$

$$\text{e.g., } \mathbf{u}_{el=1} = \underline{\mathbf{u}}(\text{edof}_{el=1}) = [u_4 \ u_5 \ u_6 \ u_{10} \ \dots \ u_{26} \ u_{27}]^T \quad (24)$$

can be extracted for each element from the global displacement vector $\mathbf{u} = [u_1 \ u_2 \ \dots \ u_{n_{dof}}]$. The underbar in the expression $\underline{\bullet}$, indicates that a quantity \bullet refers to the ordered nodal values.

2.2.3. Parametric Domain

Now, the solution field inbetween the nodal values must be interpolated. Let a local coordinate vector $\xi = (\xi_1, \xi_2, \xi_3)^T$ and the parametric domain $\mathcal{B}_\xi = \{\xi \in \mathbb{R}^3 | \xi_1, \xi_2, \xi_3 \in [-1, 1]\}$ be given. As we already performed the mapping from the current to the reference domain, $\mathcal{B}_t \rightarrow \mathcal{B}_0$ in Equation (10), by using the integration by substitution

$$\int_{\mathcal{B}_t} \bullet \, dv = \int_{\mathcal{B}_0} \bullet \, J \, dV \tag{25}$$

We must map each element to the reference domain \mathcal{B}_ξ , to perform Gaussian quadrature. In the following case, it is an affine transformation between the reference and the parametric domain,

$$\int_{\mathcal{B}_0} \bullet \, dV = \sum_{el=1}^{n_{el}} \int_{\mathcal{B}_\xi} \bullet_{el} \, J_\xi \, d\Omega \quad \text{and} \quad J_\xi = \det\left(\frac{\partial \mathbf{X}}{\partial \xi}\right) = \left[\frac{h}{2}\right]^3 \equiv \frac{dV}{d\Omega} \tag{26}$$

where h is the equidistant nodal spacing in the physical domain (see Figure 3a) and 2 is the length of the parametric domain in each direction. Without loss of generality, we set $h = 2$ in the following.

2.2.4. Ansatz Functions

The ansatz functions for both the displacement and the test function on each element are written in terms of the local coordinate vector ξ , as

$$\mathbf{u}_{el}(\xi) = \sum_i N_i(\xi) \mathbf{u}_{eli} \quad \text{and} \quad \lambda_{el}(\xi) = \sum_j N_j(\xi) \lambda_{elj} \tag{27}$$

where it is necessary to note that the entire dependency of \mathbf{u}_{el} and λ_{el} on ξ , is carried by the interpolation functions N_i only. For computational reasons, often low polynomial degree functions are used, e.g., linear Lagrangian interpolation functions, which read

$$N_i(\xi) = \frac{1}{2}(1 + s_1^i \xi_1) \frac{1}{2}(1 + s_2^i \xi_2) \frac{1}{2}(1 + s_3^i \xi_3) \quad \text{where} \quad \begin{cases} s_1^i = (-1)^i \\ s_2^i = \text{sign}(\sin(\frac{\pi}{4}(1 - 2i))) \\ s_3^i = \text{sign}(i - 4.5) \end{cases} \tag{28}$$

and $i \in \{1, \dots, 8\}$. In accordance to the node identification of Section 2.2.2, the sequence of s_1^i is $\{-1, 1, -1, 1, -1, 1, -1, 1\}$, the sequence of s_2^i is $\{-1, -1, 1, 1, -1, -1, 1, 1\}$, and the sequence of s_3^i is $\{-1, -1, -1, -1, 1, 1, 1, 1\}$. In the case of derivatives, one should note that $\nabla_X N_i(\mathbf{X}) = \nabla_\xi N_i(\xi) J_\xi = \nabla_\xi N_i(\xi) \frac{2}{h}$.

2.2.5. Strain–Displacement Matrix

With the ansatz functions at hand, and by using Equation (26), the weak problem (21)₄ reads on each element

$$\int_{\mathcal{B}_\xi} (\nabla_\xi N_i \mathbf{F}_{el}^T) : \mathbf{S}_{el} \, d\Omega = \int_{\mathcal{B}_\xi} \mathbf{B}_{el}^T \mathbf{S}_{el}^V \, d\Omega \quad \text{and} \quad \mathbf{S}_{el}^V = \mathbf{C} \mathbf{E}_{el}^V(\mathbf{u}_{el}) \tag{29}$$

A quantity called the “non-linear nodal strain–displacement matrix”

$$\mathbf{B}_i = \begin{bmatrix} F_{11} \partial_1 N_i & F_{21} \partial_1 N_i & F_{31} \partial_1 N_i \\ F_{12} \partial_2 N_i & F_{22} \partial_2 N_i & F_{32} \partial_2 N_i \\ F_{13} \partial_3 N_i & F_{23} \partial_3 N_i & F_{33} \partial_3 N_i \\ F_{13} \partial_2 N_i + F_{12} \partial_3 N_i & F_{22} \partial_3 N_i + F_{23} \partial_2 N_i & F_{32} \partial_3 N_i + F_{33} \partial_2 N_i \\ F_{11} \partial_3 N_i + F_{13} \partial_1 N_i & F_{21} \partial_3 N_i + F_{23} \partial_1 N_i & F_{33} \partial_1 N_i + F_{31} \partial_3 N_i \\ F_{11} \partial_2 N_i + F_{12} \partial_1 N_i & F_{22} \partial_1 N_i + F_{21} \partial_2 N_i & F_{31} \partial_2 N_i + F_{32} \partial_1 N_i \end{bmatrix} \tag{30}$$

is introduced, where F_{ij} are the entries of the deformation gradient \mathbf{F}_{el} , and $\partial_j \equiv \partial_{\xi_j}$ is the derivative in the j th direction. The elemental strain–displacement matrix is composed by the nodal matrices as

$$\mathbf{B}_{el} = [\mathbf{B}_{i=1}, \dots, \mathbf{B}_{i=8}] \in \mathbb{R}^{6 \times 24} \quad (31)$$

Alternatively, one can show that the elemental variation in the strain $\delta \mathbf{E}_{el} = \mathbf{B}_{el} \delta \mathbf{u}_{el}$ relates the non-linear \mathbf{B}_{el} -matrix to the variation in the elemental displacements.

2.2.6. Residual of Equilibrium Equation

Now, we can elaborate on the weak form (21) on element basis,

$$\sum_{el=1}^{n_{el}} \sum_{j=1}^8 \lambda_{elj}^T \left(\int_{\mathcal{B}_{\xi}} \mathbf{B}_{el}^T \mathbf{S}_{el}^V d\Omega - \int_{\mathcal{B}_{\xi}} N_j \tilde{\mathbf{B}}_{el} d\Omega \right) = \sum_{el=1}^{n_{el}} \sum_{j=1}^8 \lambda_{elj}^T \mathbf{R}_{el} = 0 \quad (32)$$

where the term in parentheses is identified as elemental residuum \mathbf{R}_{el} , which in turn is given by the difference between internal and external forces on that element,

$$\mathbf{R}_{el}(\mathbf{u}) = \mathbf{f}_{int} - \mathbf{f}_{ext} \in \mathbb{R}^{24} \quad (33)$$

and both, the internal and external elemental forces read

$$\mathbf{f}_{el}^{int} = \int_{\mathcal{B}_{\xi}} \mathbf{B}_{el}^T \mathbf{S}_{el}^V d\Omega \quad \text{and} \quad \mathbf{f}_{el}^{ext} = \int_{\mathcal{B}_{\xi}} N_j \tilde{\mathbf{B}}_{el} d\Omega \quad (34)$$

Since the nodal values λ_i , of the test function are arbitrary, we can find a residual expression

$$[\lambda_1 \quad \lambda_2 \quad \dots \quad \lambda_{n_{dof}}] \begin{bmatrix} \sum_{el=1}^{n_{el}} \sum_{j=1}^8 \frac{\partial \lambda_{elj}^T}{\partial \lambda_1} \mathbf{R}_{el} \\ \vdots \\ \sum_{el=1}^{n_{el}} \sum_{j=1}^8 \frac{\partial \lambda_{elj}^T}{\partial \lambda_{n_{dof}}} \mathbf{R}_{el} \end{bmatrix} = \underline{\lambda}^T \mathbf{R}(\mathbf{u}) = 0 \quad (35)$$

Practically, the assembly of the global residual vector \mathbf{R} , is given by adding the local values on the corresponding global position as

$$\mathbf{R}(\text{edof}_{el}) = \mathbf{R}(\text{edof}_{el}) + \mathbf{R}_{el} \quad \forall el \in \{1, \dots, n_{el}\} \quad (36)$$

2.2.7. Tangential Stiffness Matrix

The tangential stiffness matrix follows from a variation in the residuum,

$$\delta \mathbf{R}_{el}(\mathbf{u}) = \int_{\mathcal{B}_{\xi}} \mathbf{B}_{el}^T (\delta \mathbf{S}_{el}^V) + (\delta \mathbf{B}_{el}^T) \mathbf{S}_{el}^V d\Omega = \mathbf{K}_{el} \delta \mathbf{u}_{el} \quad (37)$$

$$\mathbf{K}_{el} = \int_{\mathcal{B}_{\xi}} \mathbf{B}_{el}^T \mathbf{C} \mathbf{B}_{el} + \mathbf{G}_{el}^T \mathbf{M}_{el} \mathbf{G}_{el} d\Omega \in \mathbb{R}^{24 \times 24} \quad (38)$$

where \mathbf{G}_{el} stores the linear derivatives of the ansatz functions,

$$\mathbf{G}_{el} = [\mathbf{G}_{k=1}, \dots, \mathbf{G}_{k=8}] \in \mathbb{R}^{9 \times 24} \quad \text{with} \quad \mathbf{G}_k = \begin{bmatrix} \partial_1 N_k \mathbf{1} \\ \partial_2 N_k \mathbf{1} \\ \partial_3 N_k \mathbf{1} \end{bmatrix} \in \mathbb{R}^{9 \times 3} \quad (39)$$

and the components of the 1st Piola–Kirchhoff stress tensor S_{ij} are stored in

$$\mathbf{M}_{el} = \begin{bmatrix} S_{11} \mathbf{1} & S_{12} \mathbf{1} & S_{13} \mathbf{1} \\ S_{21} \mathbf{1} & S_{22} \mathbf{1} & S_{23} \mathbf{1} \\ S_{31} \mathbf{1} & S_{32} \mathbf{1} & S_{33} \mathbf{1} \end{bmatrix} \in \mathbb{R}^{9 \times 9} \quad (40)$$

Again, similar to Equation (33), the assembly of the global tangential stiffness matrix reads

$$\mathbf{K}(\text{edof}_{\text{el}}, \text{edof}_{\text{el}}) = \mathbf{K}(\text{edof}_{\text{el}}, \text{edof}_{\text{el}}) + \mathbf{K}_{\text{el}} \quad \forall \text{el} \in \{1, \dots, n_{\text{el}}\} \quad (41)$$

2.2.8. Gaussian Quadrature

Equation (38) has polynomial degree $d = 3$, so exact integration of some function f , dependent on a polynomial expression of ξ ,

$$\int_{\mathcal{B}_{\xi}} f(\xi) \, d\Omega = \sum_{\text{gp}=1}^{n_{\text{gp}}} f(\xi_{\text{gp}}) w_{\text{gp}} \quad (42)$$

by summation, is given if the number of Gauss points is $n_{\text{gp}} = \frac{d+1}{2} = 2$, at positions $\xi_{\text{gp}} = \pm \frac{1}{\sqrt{3}}$ and weights $w_{\text{gp}} = 1$.

2.2.9. Newton–Raphson Method

The nodal displacement is found iteratively by using the Newton–Raphson method,

$$\underline{\mathbf{u}}^{it+1} = \underline{\mathbf{u}}^{it} - [\mathbf{K}(\underline{\mathbf{u}}^{it})]^{-1} \mathbf{R}(\underline{\mathbf{u}}^{it}) = \underline{\mathbf{u}}^{it} + \Delta \underline{\mathbf{u}}^{it} \quad (43)$$

where it is the iteration number. To calculate the displacement update $\Delta \underline{\mathbf{u}}^{it}$, we use a direct solver until $\frac{\|\Delta \underline{\mathbf{u}}^{it}\|}{\|\underline{\mathbf{u}}^{it}\|} < 0.001$ as the termination condition.

2.2.10. Compliance

The compliance of the system is defined in accordance with the strain energy as

$$c = \frac{1}{2} \underline{\mathbf{u}}^T \mathbf{K} \underline{\mathbf{u}} \quad \in \mathbb{R} \quad (44)$$

with tangential stiffness \mathbf{K} , from Equation (41). Sometimes compliance is defined without the factor $\frac{1}{2}$ [37]. In terms of an optimization problem, it relates a maximum stiffness demand by means of a minimum compliance.

2.3. Density Based Methods and Filtering Techniques

Although the term *density*, suggests that the method relies on a quantity extended in space, the density variable $x_i \forall i \in \{1, \dots, n_{\text{el}}\}$, is considered only at the element's center of mass. It is conceived as an effective quantity during the FEM calculation. The SIMP and BESO methods are based on the formulation that the density interpolates Young's modulus, see Equation (7). We first review the core idea of the SIMP method, then explain the filtering methods used in the optimization procedure, and show parallels with the BESO method.

2.3.1. SIMP Method

There are many different approaches to keep the binary system, consisting of material and void, from becoming singular in the stiffness tensor, by ascribing either a minimum density x_{min} ,

$$E_i(x_i) = x_i^p E_0 \quad x_i \in [x_{\text{min}}, 1] \quad \forall i \in \{1, \dots, n_{\text{el}}\} \quad (45)$$

or a minimum Young's modulus $E_{\text{min}} > 0$, to the voids. Within the (modified) SIMP approach the Young's modulus is given by a convex combination between the solid material (E_0) and the void material ($E_{\text{min}}0$)

$$E_i(\tilde{x}) = E_{\text{min}}(1 - \tilde{x}_i^p) + \tilde{x}_i^p E_0 \quad x_i \in [0, 1] \quad \forall i \in \{1, \dots, n_{\text{el}}\} \quad (46)$$

which is a function of a (normalized) density \tilde{x} , with penalization power $p > 1$. Here, it is important to distinguish between the (relative) element density x and the filtered (physical) density \tilde{x} , as described in the following.

2.3.2. Density Filter

According to [44], a basic linear filter density function is defined as

$$\tilde{x}_i = \sum_j w_{ij} x_j \quad \text{e.g., with conical weights} \quad w_{ij} = \begin{cases} \frac{r_{\min} - \text{dist}(i,j)}{\sum_j r_{\min} - \text{dist}(i,j)} & j \in \mathcal{N}_i \\ 0 & j \notin \mathcal{N}_i \end{cases} \quad (47)$$

where the weights should fulfill the partition of unity, $\sum_j w_{ij} = 1 \forall i$, and r_{\min} is an (user) input radius defining the neighborhood $\mathcal{N}_i = \{j : \text{dist}(i,j) \leq r_{\min}\}$. In general, the weights influence the resulting structure, and since there is no overall optimum result, they are somehow arbitrary [45]. Other filter types could be defined by Gaussian weights [44], Heaviside filter, dilate and erode filter [46], or filter based on the geometric mean [45]. Nevertheless, what is known for sure, without filtering, the optimum result tends to become a scattered structure, often referred to as a checkerboard, with thin structural parts and/or many tiny holes [45].

2.3.3. Sensitivity Filter

A similar procedure to Equation (47) is applied to the sensitivities, which are the derivatives of the objective function, and reads

$$\frac{\partial c}{\partial x_i} = \frac{1}{x_i} \sum_{j \in \mathcal{N}_i} \frac{\partial c}{\partial x_j} w_{ij} x_j \quad \forall i \in \{1, \dots, n_{el}\} \quad (48)$$

which is strictly speaking not a density filter because no filtering is conducted regarding the density itself. The sensitivities are used together with the design domain, $\mathbf{v} = [v_1, \dots, v_n]^T$ and a prescribed volume limit \bar{v} , to solve the Karush–Kuhn–Tucker (KKT) condition, which leads to an optimality condition $B_i = 1$, where

$$B_i = -\frac{\partial c(\tilde{\mathbf{x}})}{\partial x_i} \left(l_i \frac{\partial v(\tilde{\mathbf{x}})}{\partial x_i} \right)^{-1} \quad (49)$$

should be fulfilled. The value of the Lagrange multiplier l_i , satisfying the condition $v(\tilde{\mathbf{x}}(x^{new}(l_i)))$, is the only unknown, and is found by the bisection method. With this, the update reads

$$x_i^{new} = \begin{cases} \max(0, x_i - m) & x_i B_i^\eta \leq \max(0, x_i - m) \\ \min(1, x_i + m) & x_i B_i^\eta \geq \min(1, x_i + m) \\ x_i B_i^\eta & \text{otherwise} \end{cases} \quad (50)$$

where m is a positive move-limit, and η is a numerical damping coefficient.

2.3.4. BESO Method

The BESO method relies also on the penalty method of the Young's modulus, but here, the sensitivity of the objective function is assigned with the total strain energy, α_i , of the removed element,

$$\frac{\partial c}{\partial x_i} \approx \frac{\Delta c}{1} = -\alpha_i \quad \text{and} \quad \alpha_i = \frac{1}{2} \mathbf{u}_i^T \mathbf{f}_i^{int} \quad (51)$$

Then, the element sensitivity is given by the linear density filter (47), and reads

$$\tilde{\alpha}_i = \frac{\sum w_{ij} \alpha_j}{\sum w_{ij}} \quad (52)$$

To improve the convergence, [32], the sensitivity at the current iteration step (it) is averaged with that from the previous step,

$$\tilde{\alpha}_j^{(it)} \leftarrow \frac{\tilde{\alpha}_j^{(it)} + \tilde{\alpha}_j^{(it-1)}}{2}, \quad it > 1 \quad (53)$$

Introducing the two threshold constants, $\alpha_{\text{del}}^{\text{th}}$ for material removal and $\alpha_{\text{add}}^{\text{th}}$ for material addition, the update reads

$$x_i^{(it+1)} = \begin{cases} x_{\min} & \alpha_i \leq \alpha_{\text{del}}^{\text{th}} \\ 1 & \alpha_i > \alpha_{\text{add}}^{\text{th}} \\ x_i^{(it)} & \text{otherwise} \end{cases} \quad (54)$$

The threshold constants are found by the bisection method. Moreover, the target volume

$$v^{(it)} = \max\{\bar{v}, (1 - c_{\text{er}}v^{(it-1)})\} \quad (55)$$

where c_{er} is the evolutionary ratio determining the percentage of material to be removed. The evolutionary ratio is a number initialized in the previous iteration, and is zero when the target volume is reached. Then, only the topology alters.

2.4. Problem Formulation

Finally, the optimization problem to be solved reads

$$\begin{aligned} \text{find } \mathbf{x} &= [x_1, x_2, \dots, x_{n_{\text{el}}}]^T && \text{(density)} \\ \text{minimize } c &= \frac{1}{2} \mathbf{u}^T \mathbf{K} \mathbf{u} && \text{(compliance)} \\ \text{subject to } v &= \mathbf{x}^T \bar{\mathbf{v}} = \bar{v} && \text{(volume)} \\ \mathbf{R}(\mathbf{u}) &= \mathbf{f}_{\text{int}} - \mathbf{f}_{\text{ext}} = \mathbf{0} && \text{(residuum)} \\ \mathbf{K}(\mathbf{u}) &= \delta_{\mathbf{u}} \mathbf{R}(\mathbf{u}) && \text{(tangential stiffness)} \\ x_i &\in \{x_{\min}, 1\} && \text{(density range)} \end{aligned}$$

where in the non-linear case, the displacement \mathbf{u} is found iteratively, by using the Newton–Raphson method. The tilde in the expression $\tilde{\bullet}$, indicates that a quantity \bullet refers to the ordered elemental values. The optimum structure is found if a termination criterion is fulfilled, e.g., if a certain number of iterations is reached (failure) or the density/compliance difference is marginal between two iteration steps (success), as explained in the following.

2.4.1. Termination Criterion: Density Change

The first termination criterion is density-based, and states that an optimum structure is found if the change between the densities

$$\|\mathbf{x}^{\text{new}} - \mathbf{x}\|_{\infty} \leq \epsilon \quad (56)$$

according to the L_{∞} -norm is sufficiently small, $\epsilon \approx 0.001$. With this at hand, the updated structure would not change in the next iteration step regarding the previous one.

2.4.2. Termination Criterion: Compliance Change

Another termination criterion is based on the change in compliance, defined as a moving average

$$\frac{|\sum_{i=(it-9)}^{(it-4)} c_i - \sum_{j=(it-4)}^{(it)} c_j|}{\sum_{j=(it-4)}^{(it)} c_j} \leq \epsilon \quad it > 9 \quad (57)$$

Here, the size of the moving window is somehow arbitrary, and found empirically.

2.5. Chemo-Mechanically Coupled Model

If the optimum structure is found, we need a chemo-mechanically coupled material model to test the particles' performance. In [47], we formulated a multi-field model for charging and discharging of lithium-ion battery electrodes. Briefly sketched, the model is based on a multiplicative split of the deformation gradient

$$\mathbf{F} = \mathbf{F}_e \mathbf{F}_i \quad \text{where} \quad \mathbf{F}_i = J_i^{-2/3} \mathbf{1} \quad (58)$$

into an elastic (index e) and purely volumetric inelastic (index i) deformation. The inelastic part should depend on the lithium (Li) concentration c_{Li} , and reads

$$J_i \approx 1 + \bar{\Omega}(c_{\text{Li}} - c_0) \quad (59)$$

where $\bar{\Omega}$ is a normalized partial molar volume and c_0 a reference concentration. With this at hand, the total free energy density of Equation (18) is now, besides the right Cauchy-Green tensor \mathbf{C} , dependent on another field variable c_{Li} ,

$$\Psi = \Psi^{\text{ela}}(\mathbf{C}) + \Psi^{\text{con}}(c_{\text{Li}}) + \Psi^{\text{int}}(\nabla c_{\text{Li}}) \quad (60)$$

where $\Psi^{\text{ela}}(\mathbf{C})$ is the elastic strain energy, e.g., $\Psi^{\text{ela}}(\mathbf{C}) = \Psi_E$ from (18) but now with concentration dependent elastic moduli, $\Psi^{\text{con}}(c_{\text{Li}})$ is a double-well potential and $\Psi^{\text{int}}(\nabla c_{\text{Li}})$ accounts for interfacial reactions. Moreover, besides the quasi-static balance of linear momentum, the Cahn–Hilliard equation

$$\dot{c}_{\text{Li}} = \nabla \cdot (\mathcal{M} \nabla \delta_{c_{\text{Li}}} \Psi) \quad (61)$$

is an extension of Fickian diffusion, i.e., accounts for the irreversible temporal evolution of the additional concentration field and follows from mass conservation; \mathcal{M} , is called a mobility tensor. The Cahn–Hilliard equation is a fourth-order partial differential equation and needs, in the sense of finite element analysis at least, continuous differentiable ansatz functions. Therefore, the obtained optimum structure should be re-meshed by using quadratic B-Splines, and we follow the technique as proposed in [48]. Re-meshing is needed to evaluate the optimum structure in a post-process only, and thus does not affect the mesh during optimization.

3. Results

Here, we first compare the results obtained from linear and non-linear optimization. Then, we elaborate on the force limit, where the results are comparable (within a 3% deviation). With this, we show the simulation results obtained from a single force load. In the next step, we generate structures that result from random force strengths, subject to different constraints on the net force. Finally, all structures' (normalized) overlays give the most probable shape of a resistant structure to a random contact. This structure is subject to a periodic mechanical motion, and the induced chemo-mechanically coupled change in lithium concentration is studied.

3.1. Reference Parameter Definition

The optimization code listed in Appendix A, relies, according to [32], on the user input $(n_x, n_y, n_z, \bar{v}, c_{\text{er}}, r_{\text{min}})$ and some constants anchored inside the program (see Table 1). If there is no user input, the parameters from the calibration calculation from Section 3.2, are passed automatically. Moreover, the common linear density filter (47) is used in all numerical examples, but can be exchanged by the user if necessary.

Table 1. Variables (top row), their designation inside the Matlab code (middle row), and their reference values (bottom row).

E	ν	x_{\min}	p	$\bar{\nu}$	r_{\min}	c_{er}	F_0	ϵ
E	nu	xmin	penal	volfrac	rmin	er	F0	tolx
1	0.3	3×10^{-5}	1	0.5	1.5	0.02	10^{-9}	10^{-4}

3.2. Calibration

For the calibration of the optimization algorithm, we first check that the results obtained from the small strain BESO method are comparable with the small strain SIMP method, in terms of a binarized density at threshold $x_i = 0.5 \forall i \in \{1, \dots, n_{el}\}$. To this end, we choose the well-known cantilever beam, and set the number of elements to (50, 16, 4), see Figure 4a. Next, we declare a desired volume of 50% and the normalized force strength to be 10^{-9} . The convergence plot is shown in Figure 4b and is very similar to the 2D case reported in [32]. The resulting structure from the BESO method is used as input structure for the SIMP optimization calculation, with similar parameters, i.e., we adapted $E_0 = 1$, $p = 3$, $r_{\min} = 1.5$, $\bar{\nu} = 0.5$, and adjusted $E_{\min} = 3.1 \times 10^{-2}$ (see Equations (45) and (46)) and $tolx = 0.015$. Since there is almost no difference (two elements change) between the SIMP and the BESO solution at small force strengths, we declare this structure as a reference solution. Then, we increase the force strength and define a deviation D , by element-wise density comparison. Finally, we count only those elements (dark cubes) that do not match the reference solution (see Figure 4c), i.e., the higher D , the more the structure deviates from the reference solution. As expected, the higher the force strength, the higher the deviation.

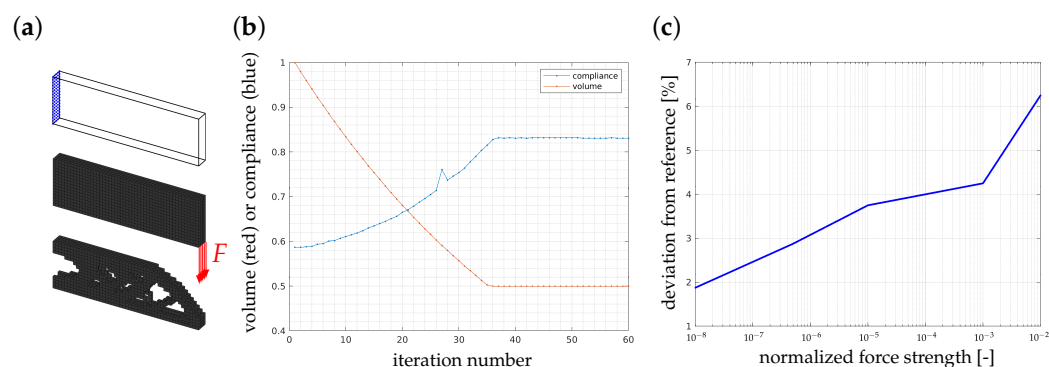


Figure 4. Optimization of a cantilever beam: (a) boundary conditions and reference optimum design, (b) evolutionary histories of the volume fraction and the compliance ($\times 10^{15}$), and (c) deviation from reference solution dependent on the force strength.

3.3. Central Single Force

Now, the reference geometry is given by a (16, 16, 16) cube, which is subject to a fixture by Dirichlet boundary conditions on the bottom (see blue dots in Figure 5a), a single force acting on top of the surface, and a prescribed volume, of 30% and 50%, respectively. The optimization converges very fast (see Figure 5c) and leads to a conical structure (see Figure 5b), which is almost independent of the force strength applied. Conical structures have already been investigated experimentally in the context of Li-ion battery anodes, by [49], and numerically by [50]. Nevertheless, this kind of structure is resistant to one-sided loadings only, and therefore, we proceed with all-round random contact in the following.

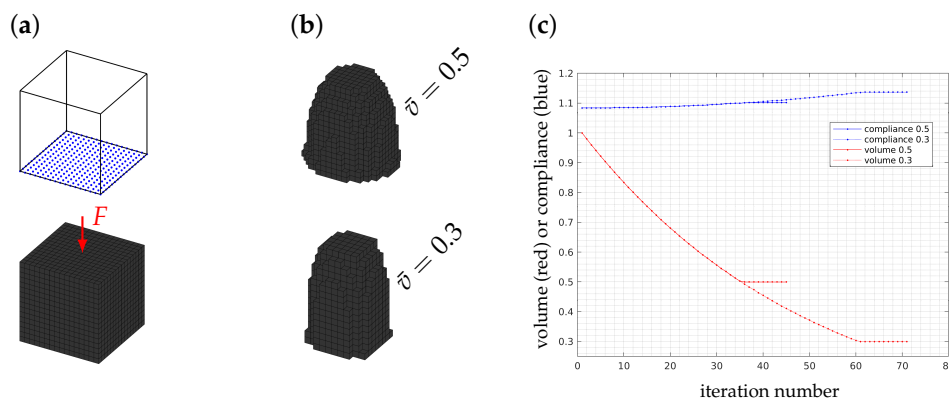


Figure 5. Optimization of a cube subjected to a single force: (a) boundary conditions, (b) optimum structures at prescribed volumes, and (c) evolutionary histories of the volume fraction and the compliance ($\times 10^{18}$).

3.4. Forces with Random Strength and Zero Net Strength

Now, we consider again the (16,16,16) cube, which is fixed at the center of mass (see blue dots in Figure 6a). We apply forces with random strength, but overall, they are constrained to zero net force (see Figure 6b). Doing so makes the resulting structures look arbitrary (see Figure 6c). The observed island phenomenon is likely due to the applied boundary conditions in the center of the geometry. Due to the randomness of the force strength, the optimum structures are not comparable if repeating the simulation. Especially in Figure 6d, we have omitted the structure’s walls, which were mostly filled with material. Therefore, we must consider a statistical interpretation of the internal structure, as explained in the following subsection.

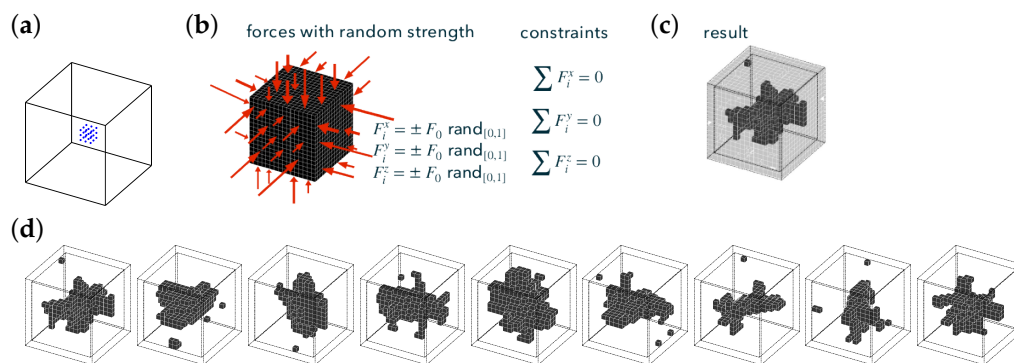


Figure 6. Optimization of a cube: (a) boundary conditions for the fixture, (b) random strength, as boundary condition, with a zero net force constraint, (c) optimum structure, and (d) more optimum structures showing different pattern.

3.5. Probability Density

Since the underlying domain is always kept the same, we can define a probability

$$P_i = \frac{\sum_{s=1}^{n_{sim}} (x_i)_s}{n_{sim}} \quad \forall i \in \{1, \dots, n_{el}\} \tag{62}$$

for each element, which indicates how often the optimized result in the specific domain is provided with material. The cube’s core has the highest probability that it must be filled with solid material, which decreases towards the cube’s corners. Instead of the prescribed volume \bar{v} , we can now consult the probability quantile as the superior optimization constraint, which we had to declare for the post-processing. Regarding the color distribution in Figure 7, the most likely structure is a ball (yellow region), very unlikely a fully filled cube

(dark blue), and a Schwarz P minimum surface delimits the transition area to an intermediate structure. The Schwarz P surface itself can be described analytically by the function

$$\cos(X_1) + \cos(X_2) + \cos(X_3) = 0 \tag{63}$$

In the following, we will mesh it as a solid and expose it to chemo-mechanical cycling.

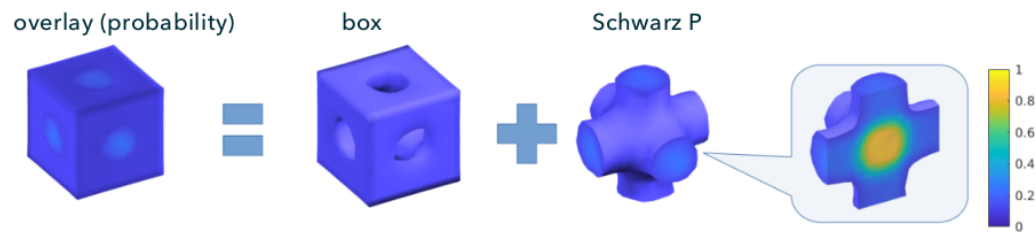


Figure 7. Color code overlay of optimization results and their decomposition into a box and a Schwarz P structure (for $P > 0.1$).

3.6. Periodic Loading of Schwarz P Structure

The topology-optimized structure is now subjected to sinusoidal cyclic loading, and an initial value problem is solved using the chemo-mechanically coupled model. In Figure 8, the concentration distribution is shown, where the concentration is pushed outward in a compressive motion and vice versa. Since the constitutive law follows the thermodynamics of irreversible processes, it can be seen that after the first mechanical cycle, the concentration distribution does not return to the uniformly distributed original state, but an induced pattern persists.

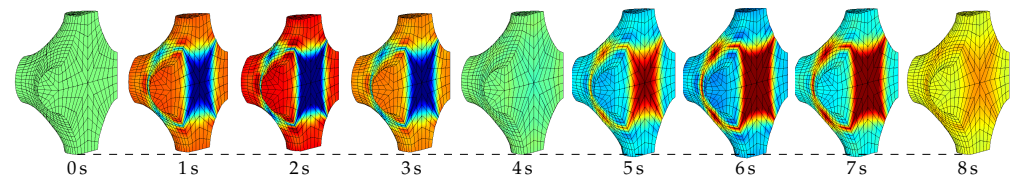


Figure 8. Concentration distribution due to compression/tension, dashed line serves for guidance.

3.7. Forces with Random Strength and Non-Zero Net Strength

Previously we assumed the constraint of a vanishing total force. Now, a net force on the object is prescribed, and then, the optimum topology changes to an eighth of a bee-shaped structure, with spikes in the diagonal corners, see Figure 9.

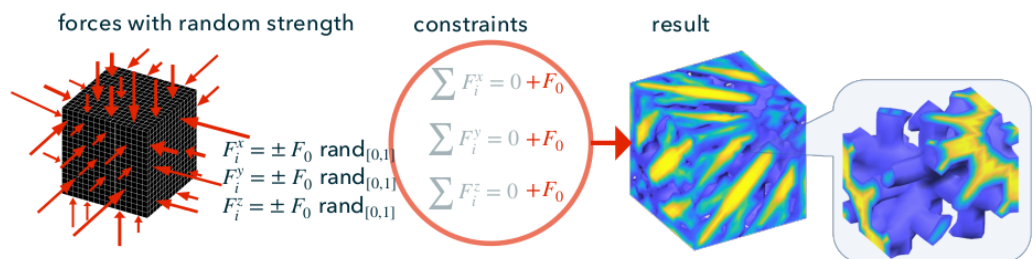


Figure 9. Optimization of a cube, subject to forces with random strength and a net force constraint.

4. Discussion

The core question of this paper, was related to the optimal geometry of a silicon anode exposed to a random contact. It is known that silicon anodes swell to multiples of their original volume. Thus, depending on the charging behavior, the interaction between the particles is somewhat random, regarding the force strength and the local position of the occurrence. We have developed and provided a compact Matlab code to

address the question of an optimal geometry that is as resistant as possible to this type of force action. The code is based on the two papers by [32,37]. The published code of the first reference is known for its particular simplicity of implementation of boundary conditions, and the second reference for its fast convergence rate, whereas the latter code had been published only in 2D. In addition, all studies we have performed using the new code, provide symmetric structures under symmetric loading, which is infrequent in the literature. Then, we subjected a cube to random loading but obtained structures challenging to interpret. However, we considered the normalized overlap as the probability density when overlapping the structures resulting from many simulations. As a result, we obtained the symmetric Schwarz P structure at a specific threshold, which has a minimum surface property. Such results sound promising in the context of electrodes, where structures with minimum surface area are desired. Furthermore, this method also yields what one would intuitively expect, e.g., a structure concentrated along the diagonal in the case of diagonal loading. Finally, the material model is chosen, so that it can be extended in the future by a crack density field, for a crack propagation study.

5. Conclusions

Here, we elaborated on large, geometrically non-linear deformations of battery anodes, intending to find an optimum (maximum stiff) electrode design when subject to random contact, in terms of random forces. The optimization technique relies on the BESO method, where the solution procedure includes non-linear finite element analysis, specific sensitivity filtering, and an improved weighting of the historical information, to ensure fast convergence. The existing 2D Matlab code reported in [32] was extended here to 3D, attached in the appendix, and applied to several design problems. Even at moderate volume fractions, the resulting topologies are hard to compare with each other. Thus, in such cases, the optimum structures are found by performing multiple simulations and interpreting their (normalized) overlap as a probability density.

Author Contributions: Conceptualization, M.W. and S.B.; methodology, M.W. and K.W.; software, M.W.; validation, S.B. and K.W.; formal analysis, M.W. and K.W.; investigation, S.B. and M.W.; resources, M.W.; writing—original draft preparation, M.W.; writing—review and editing, S.B. and K.W.; visualization, M.W. and S.B.; supervision, K.W.; project administration, K.W.; funding acquisition, K.W. All authors have read and agreed to the published version of the manuscript.

Funding: This research was funded by DFG grant number 2525/11-1.

Institutional Review Board Statement: Not applicable.

Informed Consent Statement: Not applicable.

Data Availability Statement: Data can be reproduced by using the Matlab code from Appendix A.

Conflicts of Interest: The authors declare no conflict of interest.

Abbreviations

The following abbreviations are used in this manuscript:

BESO	Bi-evolutionary structural optimization
dof	Degree of freedom
ESO	Evolutionary structural optimization
FEM	Finite element method
Li	Lithium
Si	Silicon
SIMP	Solid isotropic material with penalization

List of Symbols

The following symbols are used in this manuscript:

\bullet_{el}	• With respect to element	n, N	Normal vector
\bullet^{it}	• With respect to iteration number	p	Penalization power
\bullet^T	Transpose of •	P	Probability density
\bullet^V	Voigt notation of •	\mathbf{P}	1st Piola–Kirchhoff stress tensor
$\bar{\bullet}$	Prescribed quantity	r_{min}	Filter radius
\bullet_n	Arranged with respect to nodal values	\mathbf{R}	Residual vector
\bullet_e	Arranged with respect to elemental values	\mathbf{S}	2nd Piola–Kirchhoff stress tensor
$tr(\bullet)$	Sum of diagonal elements (trace)	t	time
$\mathbf{0}$	Zero matrix	\mathbf{t}, T	Cauchy traction vector
$\mathbf{1}$	Identity matrix	\mathbf{u}, \mathbf{U}	Displacement vector
a, A	Area	v, V	Volume
B_i	Optimality condition	v	Design domain
$\mathbf{b}, \bar{\mathbf{B}}$	Body force density	w	Weights
\mathbf{B}	Strain–displacement matrix	x, x_{min}	Density variable, minimum density
c	Compliance	\tilde{x}	Filtered density
c_0	Ref Lithium ion concentration	\mathbf{x}, \mathbf{X}	Point of a continuum
c_{er}	Evolutionary ratio	α_i	Total strain energy of removed element
c_{Li}	Lithium ion concentration	α_{th}	Threshold constant
\mathbf{C}	Right Cauchy–Green strain tensor	δ	Variational derivative
d	Polynomial degree	ϵ	Small number $\ll 1$
D	Deviation	ϵ	Small strain tensor
$edof_{el}$	edof array for a specific element	η	Damping coefficient
E	Young’s modulus	λ, μ	Lamé parameter
E_n	Total strain energy of removed element	λ	Test function
\mathbf{E}	Green–Lagrangian strain tensor	ν	Poisson number
F_0	Force strength	ξ	Local coordinate vector
f	Force	σ	Cauchy stress tensor
\mathbf{F}	Deformation gradient	Ψ	Strain energy density function
\mathbf{G}_{el}	Linear derivatives matrix	Ω	Volume (parametric domain)
h	Equidistant nodal spacing	$\bar{\Omega}$	Normalized partial molar volume
J	Jacobian	\mathcal{B}	Body (0 reference, t actual, ξ parametric)
\mathbf{K}	Stiffness matrix	$\partial\mathcal{B}$	Boundary of body
l	Lagrange multiplier	\mathcal{C}	Elasticity tensor
m	Move limit	\mathcal{M}	Mobility tensor
\mathbf{M}_{el}	Stress components matrix	\mathcal{N}	Neighborhood
n_{el}	Number of elements	∇, ∂	Partial derivative
n_{gp}	Number of Gauss points	\emptyset	Empty set
n_{sim}	Number of simulations	\cup, \cap	Union and intersection of sets
N_i	Interpolation function		

Appendix A. Matlab Code

In Listing A1, we show the condensed 3D Matlab source code with sufficient comments. Of course, this code can be accelerated at the expense of readability.

Listing A1. 3D Matlab source code for non-linear topology optimization based on the BESO method.

```

1 function [x,U]=TopOptBesoNL3D_mdpi(nelx,nely,nelz,volfrac,er,rmin)
2 %-- if no input, then use some default values:
3 if nargin<6; nelx=50; nely=16; nelz=4; volfrac=0.5; er=0.02; rmin=1.5; end
4 %-- force strength (F0)
5 F0=1e-9; E=1; nu=0.3; xmin=3e-5; penal=1; tolX=0.0001; maxloop=500;
6 vol=1; loop=0; change=1; pos=1;
7 x=ones(nely,nelx,nelz); c=zeros(1,maxloop);

```

```

8 nele=nelx*nely*nelz; ndof=3*(nelx+1)*(nely+1)*(nelz+1);
9 %-- loads, here: at right end along z-direction
10 [il,jl,kl] = meshgrid(nelx, 0, 0:nelz);
11 loadnid=kl*(nelx+1)*(nely+1)+il*(nely+1)+(nely+1-jl);
12 loaddof=3*loadnid(:)-1;
13 F=sparse(loaddof,1,F0,ndof,1);
14 %-- supports, here: at left end along y- and z-direction
15 [iif,jf,kf]=meshgrid(0,0:nely,0:nelz);
16 fixednid=kf*(nelx+1)*(nely+1)+iif*(nely+1)+(nely+1-jf);
17 fixeddof=[3*fixednid(:); 3*fixednid(:)-1; 3*fixednid(:)-2];
18 %-- get free dofs
19 freedofs=setdiff(1:ndof,fixeddof);
20 %-- edof
21 edofMat=zeros(nele,24); ID=reshape(1:ndof/3,nely+1,nelx+1,nelz+1);
22 for iz=1:nelz
23 for ix=1:nelx
24 for iy=1:nely
25     edofMat_1=ID([0,1]+iy,[0,1]+ix,[0,1]+iz);
26     edofMat_1=edofMat_1([2,4,3,1,6,8,7,5]);
27     edofMat_1=3*(edofMat_1(:)-1)' + (1:3)';
28     edofMat(pos,:)=edofMat_1(:)';
29     pos=pos+1;
30 end
31 end
32 end
33 %-- START WITH ITERATION
34 while change>tolx && loop<maxloop
35 loop=loop+1;
36 if loop>1; olddc=dc; vol=max(vol*(1-er),volfrac); end
37 %-- displacement (U), sensitivities (dc) and compliance (c) from FEA
38 [U,dc,c(loop)]=FEA(nele,ndof,edofMat,x,penal,E,nu,F,freedofs);
39 %-- filtering of sensitivities
40 dc=reshape(dc,nely,nelx,nelz); dc=check(nelx,nely,nelz,rmin,dc);
41 %-- stabilization of evolutionary process
42 if loop>1; dc=(dc+olddc)/2; end
43 %-- BESO design update
44 if loop>1; x=ADDDEL(nele,vol,dc,x,xmin); end
45 %-- convergence factor (change)
46 if loop>10; change=abs(sum(c(loop-9:loop-5))-sum(c(loop-4:loop)))/sum(c(loop-4:loop)); end
47 %-- print results
48 fprintf('It.:%4i Obj.:%10.4f Vol.:%6.3f ch.:%6.3f\n',loop,c(loop)*1e15,sum(x(:))/nele,change);
49 %-- plot densities
50 display_3D(x);
51 end
52 end
53 %-- BESO design update
54 function [x]=ADDDEL(nele,volfrac,dc,x,xmin)
55 l1=min(dc(:)); l2=max(dc(:));
56 while abs((l2-l1)/l2)>1e-5; th=(l1+l2)/2; x=max(xmin,sign(dc-th));
57 if sum(x(:))>volfrac*nele; l1=th; else; l2=th; end
58 end
59 end
60 %-- linear density filter
61 function [dcf]=check(nelx,nely,nelz,rmin,dc)
62 dcf=zeros(nely,nelx,nelz);
63 for k1=1:nelz
64 for i=1:nelx
65 for j=1:nely
66 zum=0;

```

```

67 for k2=max(k1-floor(rmin),1):min(k1+floor(rmin),nelz)
68 for k=max(i-floor(rmin),1):min(i+floor(rmin),nelx)
69 for l=max(j-floor(rmin),1):min(j+floor(rmin),nely)
70     fac=rmin-sqrt((i-k)^2+(j-l)^2+(k1-k2)^2);
71     zum=zum+max(0,fac);
72     dcf(j,i,k1)=dcf(j,i,k1)+max(0,fac)*dc(l,k,k2);
73 end
74 end
75 end
76 dcf(j,i,k1)=dcf(j,i,k1)/zum;
77 end
78 end
79 end
80 end
81 %-- FEA
82 function [U,dc,cloop]=FEA(nele,ndof,edofMat,x,penal,E,nu,F,freedofs)
83 %-- initialization of global stiffness matrix (K), residuum (R) and displacement (U)
84 K=sparse(ndof,ndof); R=zeros(ndof,1); dU=R; U=R; dc=zeros(nele,1); del=1; loop=0;
85 %-- Iteratively solve the geometric nonlinear FE balance equation
86 while del>0.001 && loop<4 % or increase for more iterations
87     cloop=0; loop=loop+1;
88     %-- loop over elements
89     for ele=1:nele
90         %-- elemental quantities
91         xe=x(ele); edof=edofMat(ele,:); Ue=U(edof);
92         [RE,KE,dce]=solver(E,nu,Ue,xe,penal);
93         %-- assembly
94         K(edof,edof)=K(edof,edof)+KE; R(edof)=R(edof)+RE; dc(ele)=dce;
95         cloop=cloop+0.5*xe^penal*Ue'*KE*Ue;
96     end
97     %-- residual, tangent and displacement
98     R=sparse(R+F); K=sparse((K+K')/2);
99     %-- direct solver
100    dU(freedofs,:)=K(freedofs,freedofs)\R(freedofs,:); U=U+dU; del=norm(dU,2)/norm(U,2);
101 end
102 end
103 %-- FE solver
104 function [RE,KE,dc]=solver(E,nu,Ue,xele,penal)
105 %-- initialization
106 RE=zeros(24,1); KE=zeros(24,24); dc=0; sq=1/sqrt(3); Y=eye(3); Z=zeros(3);
107 %-- displacements (uij) where i=number, j=direction
108 u11=Ue(1); u21=Ue(4); u31=Ue(7); u41=Ue(10); u51=Ue(13); u61=Ue(16); u71=Ue(19); u81=Ue(22);
109 u12=Ue(2); u22=Ue(5); u32=Ue(8); u42=Ue(11); u52=Ue(14); u62=Ue(17); u72=Ue(20); u82=Ue(23);
110 u13=Ue(3); u23=Ue(6); u33=Ue(9); u43=Ue(12); u53=Ue(15); u63=Ue(18); u73=Ue(21); u83=Ue(24);
111 %-- elasticity tensor (C)
112 C=xele^penal*E/((1+nu)*(1-2*nu))*[(1-2*nu)*Y+nu*(Z+1),Z;Z,(0.5-nu)*Y];
113 %-- Gaussian quadrature over 3^2=8 points and weights=1
114 for gp=1:8
115     %--sign (si) of ansatz functions
116     s1=1-2*mod(gp,2); s2=sign(sin(pi/4*(1-2*gp))); s3=sign(gp-4.5);
117     p1=1+s1*sq; m1=1-s1*sq; p2=1+s2*sq; m2=1-s2*sq; p3=1+s3*sq; m3=1-s3*sq;
118     %-- derivative of ansatz functions Ni wrt j, (dNij) where e.g. dN21=-dN11
119     dN11=-m2*m3/8;dN31= p2*m3/8;dN51=-m2*p3/8;dN71= p2*p3/8;
120     dN12=-m1*m3/8;dN22=-p1*m3/8;dN52=-m1*p3/8;dN62=-p1*p3/8;
121     dN13=-m1*m2/8;dN23=-p1*m1/8;dN33=-p1*p2/8;dN43=-m1*p2/8;
122     dN1=[dN11,-dN11,dN31,-dN31,dN51,-dN51,dN71,-dN71];
123     dN2=[dN12,dN22,-dN22,-dN12,dN52,dN62,-dN62,-dN52];
124     dN3=[dN13,dN23,dN33,dN43,-dN13,-dN23,-dN33,-dN43];
125     %-- components of deformation gradient (Fij)

```

```

126 F11=dN11*(u11-u21)+dN31*(u31-u41)+dN51*(u51-u61)+dN71*(u71-u81)+1;
127 F12=dN11*(u12-u22)+dN31*(u32-u42)+dN51*(u52-u62)+dN71*(u72-u82);
128 F13=dN11*(u13-u23)+dN31*(u33-u43)+dN51*(u53-u63)+dN71*(u73-u83);
129 F21=dN12*(u11-u41)+dN22*(u21-u31)+dN52*(u51-u81)+dN62*(u61-u71);
130 F22=dN12*(u12-u42)+dN22*(u22-u32)+dN52*(u52-u82)+dN62*(u62-u72)+1;
131 F23=dN12*(u13-u43)+dN22*(u23-u33)+dN52*(u53-u83)+dN62*(u63-u73);
132 F31=dN13*(u11-u51)+dN23*(u21-u61)+dN33*(u31-u71)+dN43*(u41-u81);
133 F32=dN13*(u12-u52)+dN23*(u22-u62)+dN33*(u32-u72)+dN43*(u42-u82);
134 F33=dN13*(u13-u53)+dN23*(u23-u63)+dN33*(u33-u73)+dN43*(u43-u83)+1;
135 F1=[F11,F21,F31]; F2=[F12,F22,F32]; F3=[F13,F23,F33];
136 %-- strain-displacement matrix (B)
137 B1= repmat( [F1;F2;F3] , 1, 8) .* reshape( repmat( [dN1;dN2;dN3] , 3, 1) , 3, 24);
138 B2= repmat( [F3;F1;F2] , 1, 8) .* reshape( repmat( [dN2;dN3;dN1] , 3, 1) , 3, 24);
139 B3= repmat( [F2;F3;F1] , 1, 8) .* reshape( repmat( [dN3;dN1;dN2] , 3, 1) , 3, 24);
140 B=[B1;B2+B3]; BT=B'; CB=C*B; SV=CB*Ue;
141 %-- elemental residuum (RE), stiffness matrix (KE), and compliance (dc) update
142 Fint=BT*SV; RE=RE-Fint; dc=dc+0.5*Ue'*Fint;
143 G=[dN11*Y, -dN11*Y, dN31*Y, -dN31*Y, dN51*Y, -dN51*Y, dN71*Y, -dN71*Y;
144     dN12*Y, dN22*Y, -dN22*Y, -dN12*Y, dN52*Y, dN62*Y, -dN62*Y, -dN52*Y;
145     dN13*Y, dN23*Y, dN33*Y, dN43*Y, -dN13*Y, -dN23*Y, -dN33*Y, -dN43*Y];
146 M=[SV(1)*Y, SV(6)*Y, SV(5)*Y; SV(6)*Y, SV(2)*Y, SV(4)*Y; SV(5)*Y, SV(4)*Y, SV(3)*Y];
147 KE=KE+BT*CB+G'*M*G;
148 end
149 end
150 %--display
151 function display_3D(rho)
152 [nely,nelx,nelz]=size(rho); cla; face = [1 2 3 4; 2 6 7 3; 4 3 7 8; 1 5 8 4; 1 2 6 5; 5 6 7 8];
153 for z=0:(nelz-1)
154 for x=0:(nelx-1)
155 for y=nely:-1:1
156 R = rho(1+nely-y,x+1,z+1);
157 if R>0.5
158     vert=[x,-z,y;x,-z,y-1;x+1,-z,y-1;x+1,-z,y;x,-z-1,y;x,-z-1,y-1;x+1,-z-1,y-1;x+1,-z-1,y];
159     patch('Faces',face,'Vertices',vert,'FaceColor',(0.2+0.8*(1-R))*[1,1,1]); hold on;
160 end
161 end
162 end
163 end
164 axis equal; axis tight; axis off; box on; view([30,30]); pause(1e-9);
165 end
166 %-- Disclaimer:
167 %-- The authors reserves all rights for the program.
168 %-- The code may be distributed and used for educational purposes.
169 %-- The authors do not guarantee that the code is free from errors, and
170 %-- they shall not be liable in any event caused by the use of the code.
171 %-- contact: marek.werner@uni-siegen.de

```

References

- Schmit, L.A. Structural design by systematic synthesis. In Proceedings of the 2nd Conference on Electronic Computation, Pittsburgh, PA, USA, 8–10 September 1960; ASCE: New York, NY, USA, 1960; pp. 105–132.
- Bendsøe, M.P.; Kikuchi, N. Generating optimal topologies in structural design using a homogenization method. *Comput. Methods Appl. Mech. Eng.* **1988**, *71*, 197–224. [[CrossRef](#)]
- Ballo, F.M.; Gobbi, M.; Mastinu, G.; Prevati, G. *Optimal Lightweight Construction Principles*, 1st ed.; Springer: Cham, Switzerland, 2021. [[CrossRef](#)]
- Czerwinski, F. Current Trends in Automotive Lightweighting Strategies and Materials. *Materials* **2021**, *14*, 6631. [[CrossRef](#)] [[PubMed](#)]
- Chen, L.; Zhang, Y.; Chen, Z.; Xu, J.; Wu, J. Topology optimization in lightweight design of a 3D-printed flapping-wing micro aerial vehicle. *Chin. J. Aeronaut.* **2020**, *33*, 3206–3219. [[CrossRef](#)]

6. Orme, M.; Madera, I.; Gschweidl, M.; Ferrari, M. Topology Optimization for Additive Manufacturing as an Enabler for Light Weight Flight Hardware. *Designs* **2018**, *2*, 51. [[CrossRef](#)]
7. Liu, S.; Hu, R.; Li, Q.; Zhou, P.; Dong, Z.; Kang, R. Topology optimization-based lightweight primary mirror design of a large-aperture space telescope. *Appl. Opt.* **2014**, *53*, 8318–8325. [[CrossRef](#)]
8. Zhu, J.; Zhou, H.; Wang, C.; Zhou, L.; Yuan, S.; Zhang, W. A review of topology optimization for additive manufacturing: Status and challenges. *Chin. J. Aeronaut.* **2021**, *34*, 91–110. [[CrossRef](#)]
9. Ismail, A.Y.; Na, G.; Koo, B. Topology and Response Surface Optimization of a Bicycle Crank Arm with Multiple Load Cases. *Appl. Sci.* **2020**, *10*, 2201. [[CrossRef](#)]
10. Matsimbi, M.; Nziu, P.K.; Masu, L.M.; Maringa, M. Topology Optimization of Automotive Body Structures: A review. *Int. J. Eng. Res. Technol.* **2021**, *13*, 4282–4296.
11. Omar, M.A. Chain Drive Simulation Using Spatial Multibody Dynamics. *Adv. Mech. Eng.* **2014**, *6*, 378030. [[CrossRef](#)]
12. Jiang, Y.; Zhan, K.; Xia, J.; Zhao, M. Topology Optimization for Minimum Compliance with Material Volume and Buckling Constraints under Design-Dependent Loads. *Appl. Sci.* **2023**, *13*, 646. [[CrossRef](#)]
13. Kang, Z.; Liu, P.; Li, M. Topology optimization considering fracture mechanics behaviors at specified locations. *Struct. Multidiscip. Optim.* **2017**, *55*, 1847–1864. [[CrossRef](#)]
14. Li, D.; Kim, I.Y. Multi-material topology optimization for practical lightweight design. *Struct. Multidiscip. Optim.* **2018**, *58*, 1081–1094. [[CrossRef](#)]
15. Rieser, J.; Zimmermann, M. Topology optimization of periodically arranged components using shared design domains. *Struct. Multidiscip. Optim.* **2021**, *65*, 18. [[CrossRef](#)]
16. Vatanabe, S.L.; Lippi, T.N.; de Lima, C.R.; Paulino, G.H.; Silva, E.C. Topology optimization with manufacturing constraints: A unified projection-based approach. *Adv. Eng. Softw.* **2016**, *100*, 97–112. [[CrossRef](#)]
17. Zhang, L.; Al-Mamun, M.; Wang, L.; Dou, Y.; Qu, L.; Dou, S.X.; Liu, H.K.; Zhao, H. The typical structural evolution of silicon anode. *Cell Rep. Phys. Sci.* **2022**, *3*, 100811. [[CrossRef](#)]
18. Roy, T.; Salazar de Troya, M.A.; Worsley, M.A.; Beck, V.A. Topology optimization for the design of porous electrodes. *Struct. Multidiscip. Optim.* **2022**, *65*, 171. [[CrossRef](#)]
19. Mitchell, S.L. *Topology Optimization of Silicon Anode Structures for Lithium-Ion Battery Applications*; California Institute of Technology: Pasadena, CA, USA, 2016. [[CrossRef](#)]
20. Bai, X.; Zhang, H.; Lin, J. A three-dimensionally hierarchical interconnected silicon-based composite for long-cycle-life anodes towards advanced Li-ion batteries. *J. Alloys Compd.* **2022**, *925*, 166563. [[CrossRef](#)]
21. Teki, R.; Datta, M.K.; Krishnan, R.; Parker, T.C.; Lu, T.M.; Kumta, P.N.; Koratkar, N. Nanostructured Silicon Anodes for Lithium Ion Rechargeable Batteries. *Small* **2009**, *5*, 2236–2242. [[CrossRef](#)]
22. Liang, B.; Liu, Y.; Xu, Y. Silicon-based materials as high capacity anodes for next generation lithium ion batteries. *J. Power Sources* **2014**, *267*, 469–490. [[CrossRef](#)]
23. Bluhm, G.L.; Sigmund, O.; Poullos, K. Internal contact modeling for finite strain topology optimization. *Comput. Mech.* **2021**, *67*, 1099–1114. [[CrossRef](#)]
24. Wu, Y.; Guo, Z.S. Concentration Distribution and Stresses in Porous Electrodes with Particle-Particle Contact. *J. Electrochem. Soc.* **2021**, *168*, 090507. [[CrossRef](#)]
25. Kristiansen, H.; Poullos, K.; Aage, N. Topology optimization for compliance and contact pressure distribution in structural problems with friction. *Comput. Methods Appl. Mech. Eng.* **2020**, *364*, 112915. [[CrossRef](#)]
26. Niu, C.; Zhang, W.; Gao, T. Topology optimization of elastic contact problems with friction using efficient adjoint sensitivity analysis with load increment reduction. *Comput. Struct.* **2020**, *238*, 106296. [[CrossRef](#)]
27. Lu, B.; Zhao, Y.; Feng, J.; Song, Y.; Zhang, J. Mechanical contact in composite electrodes of lithium-ion batteries. *J. Power Sources* **2019**, *440*, 227115. [[CrossRef](#)]
28. Sigmund, O. A 99 line topology optimization code written in Matlab. *Struct. Multidiscip. Optim.* **2001**, *21*, 120–127. [[CrossRef](#)]
29. Da, D.; Xia, L.; Li, G.; Huang, X. Evolutionary topology optimization of continuum structures with smooth boundary representation. *Struct. Multidiscip. Optim.* **2018**, *57*, 2143–2159. [[CrossRef](#)]
30. Fu, Y.F.; Rolfe, B.; Chiu, L.; Wang, Y.; Huang, X.; Ghabraie, K. SEMDOT: Smooth-edged material distribution for optimizing topology algorithm. *Adv. Eng. Softw.* **2020**, *150*, 102921. [[CrossRef](#)]
31. Huang, X.; Li, W. Three-field floating projection topology optimization of continuum structures. *Comput. Methods Appl. Mech. Eng.* **2022**, *399*, 115444. [[CrossRef](#)]
32. Han, Y.; Xu, B.; Liu, Y. An efficient 137-line MATLAB code for geometrically nonlinear topology optimization using bi-directional evolutionary structural optimization method. *Struct. Multidiscip. Optim.* **2021**, *63*, 2571–2588. [[CrossRef](#)]
33. Zhu, B.; Zhang, X.; Zhang, H.; Liang, J.; Zang, H.; Li, H.; Wang, R. Design of compliant mechanisms using continuum topology optimization: A review. *Mech. Mach. Theory* **2020**, *143*, 103622. [[CrossRef](#)]
34. Buhl, T.; Pedersen, C.B.W.; Sigmund, O. Stiffness design of geometrically nonlinear structures using topology optimization. *Struct. Multidiscip. Optim.* **2000**, *19*, 93–104. [[CrossRef](#)]
35. Wang, F.; Lazarov, B.S.; Sigmund, O.; Jensen, J.S. Interpolation scheme for fictitious domain techniques and topology optimization of finite strain elastic problems. *Comput. Methods Appl. Mech. Eng.* **2014**, *276*, 453–472. [[CrossRef](#)]

36. Xue, R.; Liu, C.; Zhang, W.; Zhu, Y.; Tang, S.; Du, Z.; Guo, X. Explicit structural topology optimization under finite deformation via Moving Morphable Void (MMV) approach. *Comput. Methods Appl. Mech. Eng.* **2019**, *344*, 798–818. [[CrossRef](#)]
37. Liu, K.; Tovar, A. An efficient 3D topology optimization code written in Matlab. *Struct. Multidiscip. Optim.* **2014**, *50*, 1175–1196. [[CrossRef](#)]
38. Holzapfel, G. *Nonlinear Solid Mechanics: A Continuum Approach for Engineering*; Wiley: Hoboken, NJ, USA, 2000. [[CrossRef](#)]
39. de Borst, R.; Crisfield, M.A.; Remmers, J.J.C.; Verhoosel, C.V., Non-linear Finite Element Analysis. In *Non-Linear Finite Element Analysis of Solids and Structures*; John Wiley & Sons, Ltd.: Hoboken, NJ, USA, 2012; Chapter 2, pp. 31–62. [[CrossRef](#)]
40. Sautter, K.B.; Meßmer, M.; Teschemacher, T.; Bletzinger, K.U. Limitations of the St. Venant–Kirchhoff material model in large strain regimes. *Int. J. Non-Linear Mech.* **2022**, *147*, 104207. [[CrossRef](#)]
41. Ogden, R.W.; Hill, R. Large deformation isotropic elasticity – on the correlation of theory and experiment for incompressible rubberlike solids. *Proc. R. Soc. Lond. A. Math. Phys. Sci.* **1972**, *326*, 565–584. [[CrossRef](#)]
42. Miehe, C. Aspects of the formulation and finite element implementation of large strain isotropic elasticity. *Int. J. Numer. Methods Eng.* **1994**, *37*, 1981–2004. [[CrossRef](#)]
43. Hartmann, S. *The Class of Simo & Pister-Type Hyperelasticity Relations*; Technical Report Series; Clausthal University of Technology: Clausthal-Zellerfeld, Germany, 2010.
44. Bruns, T.E.; Tortorelli, D.A. Topology optimization of non-linear elastic structures and compliant mechanisms. *Comput. Methods Appl. Mech. Eng.* **2001**, *190*, 3443–3459. [[CrossRef](#)]
45. Svanberg, K.; Svärd, H. Density filters for topology optimization based on the Pythagorean means. *Struct. Multidiscip. Optim.* **2013**, *48*, 859–875. [[CrossRef](#)]
46. Sigmund, O. Morphology-based black and white filters for topology optimization. *Struct. Multidiscip. Optim.* **2007**, *33*, 401–424. [[CrossRef](#)]
47. Werner, M.; Pandolfi, A.; Weinberg, K. A multi-field model for charging and discharging of lithium-ion battery electrodes. *Contin. Mech. Thermodyn.* **2021**, *33*, 661–685. [[CrossRef](#)]
48. Werner, M.; Weinberg, K. B-Spline meshing for high-order finite element analyses of multi-physics problems. *Tech.-Mech.-Eur. J. Eng. Mech.* **2021**, *41*, 1–11. [[CrossRef](#)]
49. Berla, L.A.; Lee, S.W.; Ryu, I.; Cui, Y.; Nix, W.D. Robustness of amorphous silicon during the initial lithiation/delithiation cycle. *J. Power Sources* **2014**, *258*, 253–259. [[CrossRef](#)]
50. Werner, M.; Weinberg, K. Towards structural optimization of lithium battery anodes. *PAMM* **2018**, *18*, e201800227. [[CrossRef](#)]

Disclaimer/Publisher’s Note: The statements, opinions and data contained in all publications are solely those of the individual author(s) and contributor(s) and not of MDPI and/or the editor(s). MDPI and/or the editor(s) disclaim responsibility for any injury to people or property resulting from any ideas, methods, instructions or products referred to in the content.